Bubble stabilization by the star-nosed mole

Alexander B. Lee and David L. Hu

Phys. Rev. Fluids **3**, 123101 — Published 6 December 2018

DOI: 10.1103/PhysRevFluids.3.123101

Bubble Stabilization by the Star-Nosed Mole

Alexander B. Lee[1] and David L. Hu[2,1*]
Schools of Biological Sciences[1] and Mechanical Engineering[2]
Georgia Institute of Technology, Atlanta, GA 30332
(Dated: November 7, 2018)

Star-nosed moles sniff for prey underwater by rapidly exhaling and inhaling bubbles that in turn capture odors on their surface. While the sniff lasts only a tenth of a second, speed alone cannot explain how the star-nosed mole so reliably sucks the bubble back in before pinch-off occurs. In this combined experimental and theoretical study, we elucidate how the unique shape of the nose stabilizes underwater bubbles. The fleshy arms of the mole's star are separated by an average of $16^\circ \pm 9$ degree increments. We laser-cut plastic stars of various angles between the arms and tilt them by hand to find the angle at which a trapped sessile bubble is released. A bubble trapped beneath the star bulges through the gaps, enabling the plastic star to retain the bubble when tilted up to 7 degrees, which is 40% greater than that of a flat plastic sheet. Using a semi-empirical model, we show two regimes where a bubble escapes. If the gap width is wider than the capillary length, buoyancy forces pull the bubble up through the gap. If the gap width is too small, the bubble does not sufficiently anchor itself in place. We show order of magnitude agreement between biological measurements, plastic star experiments, and theory, suggesting we correctly identified the mechanism for the star retaining bubbles. This study may lead to new ways of stabilizing cm-scale bubbles for underwater chemical sensing.

Keywords: sniffing, bubble

I. INTRODUCTION

Chemical sensors are not amphibious: they are deployed in either a liquid or gas phase, but not both [1]. The same limitation holds for our noses. We cannot smell underwater, and it was once believed that aquatic mammals also had a poor sense of smell underwater [2]. A number of small semi-aquatic mammals, however, have evolved ingenious ways to adapt their noses to locate food underwater. In this study, we present design considerations for these amphibious noses.

Smelling underwater begins with an exhale of a bubble. When the bubbles contacts a food item, it gathers odorant molecules, which otherwise would not make their way past the air-water barrier in the animal's nose. The bubble is then inhaled before it has a chance to pinch off and escape. **Figure 1** shows the star-nosed mole (*Condylura cristata*), the American water shrew (*Sorex palustris*) [3], and the Russian desman (*Desmata moschata*) [4], all of which sniff bubbles on a timescale of 0.07 - 0.1 seconds. The inhalation flow rates of these semi-aquatic mammals range from 0.7 - 2 mL/s, approximately twice as fast as same-sized terrestrial counterparts [5].

From hereon, we will focus our attention on the star-nosed mole, the most documented of these underwater sniffers (See **Figure 2a**). The mole's behavior allows the odor receptors in it's nose to stay dry, relying on the bubble's rapidly generated surface area as a medium to transport odor. Imitating this underwater sniffing would be an important first step towards employing gas sensors in aquatic environments. However, little is known about how to stabilize underwater bubbles larger than the capillary length, the length scale at which bubbles generally pinch off. Below we review how bubbles pinch-off and are stabilized by rough surfaces.

Bubble pinch-off has been studied in a number of contexts. As the neck of a bubble shrinks below some critical length scale [6][7], capillary forces irreversibly drive pinch-off, often quite quickly. In bubble formation from a downward nozzle, centimeter-scale bubbles, similar in size to that generated by the star-nosed mole, can pinch off in time-scales of 76 ms [8], three times as fast as the blink of an eye.

One way to delay pinch-off is to use rough substrates to stabilize the bubble. Microscopic surface roughness known as asperities can grab hold of a bubble's edge, called its contact line, leading to the bubble exhibiting a range of contact angles, a phenomenon called contact angle hysteresis. This hysteresis can hold drops and bubbles in place, even on vertical surfaces [9–12]. This phenomenon can only pin drops on the size of the capillary length, an equivalent volume of a few microliters, orders of magnitude smaller than the 0.1 mL volume of the star-nosed mole bubble[2].

Larger bubbles can be trapped by increasing the surface roughness to the extent that it obtains a Cassie-Baxter state, which makes it energetically unfavorable to displace the bubble and wet the surface [13]. Diving beetles and spiders employ densely packed hydrophobic hair to carry bubbles with them so they can breathe underwater [14, 15]. Their rough, hydrophobic surfaces are energetically costly to wet, allowing the maintenance of an air bubble of up to 3 mL in volume [13, 15, 16]. While it is possible that the microscopic surface features of the star-nosed mole may help retain bubbles, we will focus on its macroscopic features.

* hu@me.gatech.edu

In this study, we investigate the mechanism by which the star-nosed mole stabilizes its exhaled bubbles. We begin in §2 with our experimental methods for building and testing plastic stars that mimic that of the star-nosed mole. In §3, we present a semi-empirical model that elucidates the bubble-stabilizing abilities of these stars. We proceed in §4 with our experimental results, showing anatomical measurements and testing with our plastic stars. We discuss the implications of our work in §5 and conclude in §6.

II. EXPERIMENTAL METHODS

A. Measuring the star-nosed mole

We obtain three photographs of live star-nosed moles from the author of a previous study [17] (See Supplementary Materials Figure 1). The star-nosed mole has 22 conical fleshy appendages radiating from two nostrils, as shown in **Figure 2a**. To characterize the spacing between these appendages, we measure the gap angle, or the angle between the edges of two consecutive appendages, as illustrated in **Figure 2b**. The outermost section is chosen so that the gap angle accurately describes the width of the gap where the spacing is widest. The wider the gap, the more likely buoyancy can begin to dominate over surface tension forces. In **Figure 2b**, appendages 9 and 10 are an example of overlapping appendages and are not considered in our measurements.

B. Star fabrication

Plastic stars are designed in Solidworks. We begin with a circular disc of radius 20 mm. We then cut a central hole of radius $R_{nozzle} = 0.75$ mm, which corresponds to the dimensions of the syringe's nozzle. Around this hole, a ring of solid plastic, of outer radius $R = 3.5$ mm forms the center of the star. Triangular arms are cut extending from this ring, by considering both the gap angles desired and the strength of the material. Ultimately, we designed 5 arm designs, with gap angles θ of 0°, 3°, 8°, 15°, and 20°, respectively, as shown in **Figure 3b**. Note that a gap angle of 0° denotes a complete disc with no gaps. **Figure 3c** shows the relationship between the number of gaps n and the gap angle θ of the star. The stars we designed are represented by the blue points. Our first constraint is based on the strength of the material. Each arm of the star must have a minimum width of $L = 2$ mm so that it is not melted off during the laser-cutting process. This constraint may be written

$$\left(\frac{2\pi}{n} - \theta\right) R > L, \tag{1}$$

and is shown by the red dashed line in **Figure 3c**. As we found from experience, any stars that fall above this dashed line will break, at least if they are constructed from transparency sheet material.

The other constraint is on the ability of the stars to contact the bubble. In our preliminary tests, we found that we need as many gaps as possible to ensure that the bubble is forced to interact with the gaps. Moreover, we also desire an even number of gaps to maintain both front-back and left-right symmetry of the star. To determine the number of gaps cut into the star, we start at the fabrication limit and choose n to be the highest even integer below that curve. This results in stars with 6-10 arms rather than 22 arms, as in the star-nosed mole. In §3, we will use the following relationship between number of gaps and the gap angle:

$$n = -\frac{1}{3}\theta + 11. \tag{2}$$

This relationship is the best fit line considering the 3° and 15° stars, and is shown by the solid black line in **Figure 3c**.

To fabricate the stars, we begin with overhead projector transparency sheets composed of cellulose acetate. The material chosen is hydrophilic, as shown by the contact angle of $\xi = 54°$ in the inset of **Figure 4a**. We cut the star patterning using a laser cutter (Trotec Speedy 3000) into the various shapes shown in **Figure 3b**. A star is then super-glued onto a 3-mL syringe, which is in turn tied to the arm of a protractor so that it can freely swing in one plane. We orient the star so that the gaps of the star maintain symmetry both in this plane (left-right symmetry) and perpendicular to the plane (front-back symmetry, or symmetry into and out of the page in **Figure 4a**). Front-back symmetry is preferred because it allows us to accurately characterize the bubble shape from a single view, and to perform modeling with fewer variables. Left-right symmetry is maintained because we perform tilting experiments both to the left and to the right in order to obtain more data from the same star.

To demonstrate the stabilizing physics of the stars in an alternate way, we also fabricate a disc with no gaps that deforms the bubbles in a two-dimensional manner, as shown in **Figure 7**. A plastic disc is creased at a distance 3.5 mm from the center of the nozzle. The crease is made so that the disc exhibits a bend of angle $\zeta = 15°$.

C. Bubble stability experiments

With the star submerged $z = 20$ mm below the water's surface, we use syringe markings to control inflating bubbles to volume $V_t = 0.7$ mL. As a test of the bubble's stability, we slowly tilt the syringe until we discover the angle ϕ to the vertical at which the bubble pinches off (See **Figure 4a**). To account for imperfections in the star, tilting is performed in both the clockwise and counter-clockwise directions, and the average tilt angle ϕ value is reported.

As the bubble is tilted, it begins to slide. On one edge of the bubble, its contact line advances. This half of the bubble is denoted the advancing side and is highlighted in red in **Figure 6b** and **Figure 7b**. The opposite side is denoted the receding side, and is highlighted in blue in **Figure 6b** and **Figure 7b**. When the bubble escapes, it escapes in the advancing direction.

The bent disc discussed in the previous section is tested in a similar manner. In this case, the bubble is not stable at $\phi = 0$ degrees. Therefore, we carefully blow the bubble while simultaneously tilting the system so that the bubble is in contact with both the receding slope and the advancing slope. The system is then further tilted towards the advancing side to find the maximum tilt angle where the bubble pinches off.

D. Measuring bubble deformation

Considering the advancing side first, the bubble radius may be written as the central plastic disc radius R plus some incremental distance, ΔR_a, as shown in **Figure 5d**. By etching 1 mm markings on the edges of the star, we measure the motion of the bubble's contact lines for different tilt angles, ϕ, using a star with gap angles of $\theta = 8°$ as that is the median gap angle. The red points in **Figure 5e** show the change in radius of the advancing side of the bubble, ΔR_a, as a function of tilt angle. The associated changes, ΔR_r on the receding side of the bubble are shown in blue triangles. The blue and red lines show the linear least squares best fit, which are

$$\Delta R_a = \alpha + \beta\phi \ (R^2 = 0.5) \tag{3}$$

for the advancing side, and

$$\Delta R_r = \alpha - \gamma\phi \ (R^2 = 0.3). \tag{4}$$

for the receding side, where ΔR_a and ΔR_r are given in mm, ϕ in degrees, and $\alpha = 4$ mm, $\beta = 0.7\frac{mm}{degree}$, and $\gamma = 0.3\frac{mm}{degree}$. The non-equality of the slopes β and γ indicate that the bubble is not just sliding but also deforming. Specifically, the bubble is stretching as it rises. Visually, the fits given in Equation (3) and Equation (4) follow the data well, as shown in **Figure 5e**. The goodness of fit R^2 values are low, due to data standard deviation being large relative to β and γ,as the R^2 value is a metric of how much better the linear regression is as a predictor than a horizontal line at the data's mean. More importantly, the Root Mean Squared Error (RMSE) is 1 mm for both the advancing and receding regressions. The trends from our theory are not significantly changed by this magnitude of error.

In our next section, we use our empirical measurements of bubble deformation in a theoretical model for predicting the tilt angle at which the bubble will escape the star.

III. THEORY

Our theory predicts pinch-off to occur when one of two conditions is broken. We consider each condition in turn.

A. Pinch-off for large gap angles

For large gap angles, pinch-off occurs when buoyancy forces dominate capillary forces. This occurs when the width of the gap is greater than the capillary length [18], $\lambda_c = \sqrt{\frac{\sigma}{\Delta\rho g}}$ where σ is the surface tension between two fluids, $\Delta\rho$ is the difference in density between the two fluids, and g is the acceleration due to gravity. For air bubbles in water, the capillary length is λ_c= 2.7 mm. Thus, if a region of the bubble is exposed to a gap width larger than λ_c, the bubble will escape.

Bubbles that are inflated below the star assume a plate shape, similar to a puddle of water, due to the balance of surface tension forces and buoyancy at a depth of $z = 20$ mm. Consider a plate-shaped bubble radiating from the nozzle as shown in the oblique view of the bubble in **Figure 5a**, and from the top view in **Figure 5b**. **Figure 5c** shows the syringe is tilted $\phi = 4°$, and as a consequence, the bubble's advancing edge slides a distance of 1 mm from its original position shown by the dashed red lines. The bubble's advancing edge, however, travels a greater distance, indicating that the bubble has deformed.

The deformation of the bubble is due to its rising, and then resettling into a position where it has a lower gravitational potential energy. Using theory to determine the deformation of the bubble would require consideration of its three-dimensional shape, which is beyond the scope of this paper. We thus proceed by describing the bubble deformation empirically, and using it as input parameters to our model. Considering the advancing side first, the bubble radius may be written as the central plastic disc radius R plus some incremental distance, ΔR, as shown in **Figure 6a**. We neglect consideration of the receding side of the bubble because bubbles generally escape through the advancing side.

As the bubble is tilted further, it encounters an increasingly wider gap at the advancing side, as shown in **Figure 6a**. The blue hashed region indicates the bubble, which intersects the two consecutive arms of the star holding it in place. At this intersection, the arms are separated by a gap width $2(R + \Delta R_a)\tan\frac{\theta}{2}$. The bubble is stable as long as this gap width is less than the capillary length:

$$2(R + \Delta R_a)\tan\frac{\theta}{2} \leq \epsilon\lambda_c \tag{5}$$

where ϵ is a numerical prefactor, that accounts for the bubbles pinching off at length scales directly correlated to the capillary length, as is the case in a number of context [19, 20]. Preliminary experiments, expanding bubbles under horizontal stars, with gap angles of $\theta = 3°$, $8°$,

15°, and 20°, indicate that the prefactor $\epsilon \approx 1$. Thus from hereon ϵ will be omitted from equations. Applying our empirical measurements of ΔR_a in Equation (3), we rewrite Equation (5) relating ϕ to θ and solve for ϕ.

$$\phi \leq \frac{1}{\beta}\left(\frac{\lambda_c}{2\tan\frac{\theta}{2}} - R - \alpha\right) \tag{6}$$

This equation can be used to predict the maximum ϕ with respect to θ (dotted red curve, **Figure 4b**). This shows agreement with our experimental data when the gap angle θ is 15° and 20°, shown on the right hand side of **Figure 4b**. This concludes our analysis of stars of large gap angles; we now turn to stars of small gap angles.

B. Pinch-off for small gap angles

We begin with an an illustrative but more intuitive problem. Consider a weight sliding down a ramp with no friction. When the ramp is flat, no counterweight is needed. However, with any level of inclination, a counterweight is needed for equilibrium, as shown in **Figure 6c**. The same physics holds for the bubble trapped underneath a tilted star. Instead of gravitational force, two buoyancy forces act to pull the bubble in opposite directions. One force, $\rho g V \sin\phi$, is oriented parallel to the arms of the star, where V is the volume of the bubble in the red hashed region on the right of **Figure 5d** and **Figure 6b**. The other force, $\rho g v$, arises due to the bubble attempting to rise through the gaps on the receding side of the star. The buoyancy force on a body is caused by a difference in hydrostatic pressure above and below the volume, as has been done with bubbles extruded from a hole in [21]. Thus, we take v to be the entire section of the bubble denoted by the blue hashed region on the left of **Figure 5d** and **Figure 6b**. For these forces to balance, we require

$$\rho g V \sin\phi \leq \rho g v. \tag{7}$$

We proceed by determining the volumes v and V. We write the volume $v = v_1 + v_2$ where the volumes v_1 and v_2 are labelled in **Figure 6b**. We approximate the region v_1 as a pyramid, requiring the area of the base and the maximum height of the bubble to calculate its volume. The base is written as

$$b = \frac{\theta}{2\pi}[\pi(\Delta R_r + R)^2 - \pi R^2]. \tag{8}$$

If there are no gaps, then $\theta = 0$, and there is no counterweight bubble.

To find the height of v_1, we first calculate the curvature of the bubble rising through the gap according to the Young-Laplace equation

$$C = \frac{\Delta p}{\sigma} \tag{9}$$

where σ is the surface tension at an air-water interface and Δp is the difference in pressure between the surrounding water and bubble, $\Delta p = \Delta\rho g z$. From photographs, we measured the bubble angle at the plastic-water-bubble interface to be $\psi = 127°$. If we consider the cross-section of this volume as a concatenated circle, then we get the height

$$h = \frac{1 + \cos\psi}{C}. \tag{10}$$

The height h, was also measured from photographs (see Supplementary Materials Figure 2) and was found to be similar to our theoretical calculation. With h, we calculate the volume of the bubble peeking out through a gap in the star

$$v_1 = \frac{1}{3}bh. \tag{11}$$

To calculate v_2, we approximate the entire bubble below the star to be the shape of a cylinder. In that case,

$$v_2 = bd \tag{12}$$

where d is the depth of the cylinder. This depth is given by the contact angle ξ and the capillary length λ_c[22][23]

$$d = \sqrt{2(1 - \cos(\pi - \xi))\lambda_c^2}. \tag{13}$$

With values for v_1 and v_2, it is simple to calculate v, keeping in mind that the volume of bubbles in the receding half of the gaps act as counterweights. The remaining volume of the total is V, whose buoyant force is the cause of pinch off

$$v = \frac{n}{2}(v_1 + v_2) \tag{14}$$

$$V = V_t - v \tag{15}$$

If we substitute equation 15 into equation 7 we have

$$\rho g(V_t - v)\sin\phi \leq \rho g v. \tag{16}$$

We can then substitute Equation (11) and Equation (12) into Equation (14) to get an expression for v and then substitute Equation (14) into Equation (16).

$$\left(V_t - \frac{n}{2}\left(\frac{1}{3}bh + bd\right)\right)\rho g \sin\phi \leq \left(\frac{n}{2}\left(\frac{1}{3}bh + bd\right)\right)\rho g \tag{17}$$

where b is a function of both the gap angle θ and tilt-angle ϕ. Equation 17 gives this relationship between ϕ and θ, shown by the dashed red curve in **Figure 4b**.

IV. RESULTS

Videos of star-nosed moles sniffing[3] show that when the star-nosed mole sniffs underwater, it often tilts its head from side to side. The driving idea behind this study is that the shape of the star helps stabilize the bubble while it is tilted.

We first consider the dimensionless Bond number of our system, which relates the buoyancy to surface tension forces. The Bond number may be written

$$Bo = \frac{\Delta\rho g D_{eq}^2}{\sigma} \tag{18}$$

where $\Delta\rho$ is the difference in density between the water and air, g is the gravitational acceleration, σ is the interfacial surface tension between water and air, and $D_{eq} = \left(\frac{6V_t}{\pi}\right)^{1/3}$ is the equivalent spherical diameter of a bubble of volume V_t [24]. For bubbles of volume $V_t = 0.7$ mL, the Bond number is 16, suggesting that buoyancy forces are dominant. This number also indicates that the bubble is highly unstable. This is ultimately why bubbles can only be tilted to less than $\phi_c = 10$ degrees before they escape. If we consider gravity in our tilting system to be $g \sin\phi_c$, then the Bond number is 3, showing that the tilt angle of $\phi_c = 10°$ marks the transition between surface tension-dominated to buoyancy-dominated regimes. The Bond number is greater than 1, suggesting that the bubbles should be released. However, this is because the dimensionless group does not take into account the counterbalancing effect of the receding gaps.

To understand how the star shape holds onto bubbles, we begin with a simple counterexample. Consider a bubble held by a flat plastic disc as in **Figure 8a**. We tilt the disc slowly and find that at a tilt angle of $\phi = 4.5° \pm 1.5°$ to the vertical, the bubble is released. For the bubble to release, the buoyancy force on the bubble $\rho g V_t \sin\theta$ must exceed the surface tension force at the perimeter of the nozzle, $2\sigma\pi R_{nozzle}$, where R_{nozzle} is the radius of the syringe nozzle [18][19] (See **Figure 6d**). This relationship predicts that a flat plastic disc can be tilted $\phi = 3°$, which is on the same order as our experimental result. The problem with this flat disc is that there are no gaps for the bubble to rise through. These gaps allow for buoyancy forces similar to **Figure 6c** that provide counterbalance.

To demonstrate the importance of counterbalance, we perform a stability tilting experiment with a bent disc. The bend at an angle of $\zeta = 15°$ allows part of the bubble to peek over the receding slope as shown in **Figure 7**. As a result, the disc can be tilted up to $\phi = 10°$, which is more than double the values found for the flat disc. Moreover, both discs are made of the same material, indicating that differences in geometry can make a big difference in the stability of the bubble (**Figure 8**). If we assume equal volume of bubble on both the receding and advancing slopes of the plastic, then we maintain equilibrium under the following condition (See **Figure 7**b)

$$\sin(\phi) = \sin(\zeta - \phi). \tag{19}$$

Solving for ϕ, we find that the system can tilt 8°. This is comparable to the maximum tilt angle of 10° found in our experiment. We will apply similar principles to understand how the star-shaped nose increases stability of the bubble.

We proceed by looking to the star-nosed mole for inspiration, and examining the shape of the nose. When the bubble is exhaled, it is temporarily entrapped by the appendages and bulges through the gaps of the star (see **Figure 1a**). Therefore, we focus on the angles θ of these gaps, as defined in **Figure 2b**. **Figure 2c** shows a histogram of the gap angles from the three star-nosed mole photos. The histogram does not show a normal distribution, but is instead bimodal due to the ventral parts of the star having more closely spaced arms. This may have to do with the mechano-sensing role that these lower appendages play [17]. The average gap angle is 16±9° (N = 49 arms counted on 3 moles). Due to the large standard deviation, we conclude that the arms are of order 10° apart, a number which we try to rationalize using experiments with our plastic stars.

We simulate the head-tilting behavior of the mole by tilting homemade stars (See **Figure 4a**) from the vertical, thus challenging their ability to hold onto the bubble. **Figure 4b** shows the relationship between the gap angle θ and the maximum tilt angle before pinch-off ϕ. Among our five stars, the 8° and 15° stars exhibit the highest stability, holding the bubble until they are tilted to nearly 8°. This is about 150 percent higher than the lowest performing star, the 20° star. Moreover, the arms are clearly useful in holding onto the bubble. The best performing stars can hold onto bubbles at angles that are almost twice as large as a flat plate. Moreover, they are more robust than the bent plate we initially discussed. The bent plate can only hold onto bubbles when tilted in a single direction. On the other hand, the stars with multiple arms have more degrees of symmetry and thus more directions that they can be tilted before the bubble is released.

We laser-cut plastic stars of varying gap angles and performed experiments to determine their maximum degree of tilting before releasing the bubble. In §3, we gave theoretical predictions of conditions for pinch off, shown by equations 6 and 17. We have shown that larger gaps exceed the capillary length very quickly, allowing the buoyant forces to dominate over surface tension forces keeping the bubble in place (Equation 6). Small gaps fall out of equilibrium as the portion of bubble rising through the gaps is insufficient to act as counterbalance (Equation 17). According to our theory, the optimal gap angle would be $11° \pm 3°$.

V. DISCUSSION

In static tilting experiments, we showed how a star-geometry surface can add stability to a sessile bubble and that there is an optimal gap size, represented by the gap angle θ, that allows the sessile bubble to be stable at a higher tilting angle ϕ. Bubbles can slip through large gaps when the gap width is greater than the capillary length. Bubbles also fall out of static equilibrium when the gap is too small, due to the smaller counterweight effect from the bubble in receding side gaps.

The size of the gaps between the appendages in the mole's star-nose vary greatly with an average gap angle of 16°. However, the distribution of gap angles show that most of the gap angles from the photos were either much lower or much higher than this value. When comparing the optimal physics to that of the biological system, it is important to keep in mind that these appendages also have a role in tactile sensing. The roles of tactile sensing and bubble stability encompassed in the same organ can lead to evolutionary trade-off and it would be a mistake to assume that a given organ would necessarily be optimized to any one role [25].

While this study set out to show the role of the mole's star-nose, our experiments cannot confirm if the mole necessarily uses the physics we have described to stabilize bubbles during underwater sniffing. Even so, we believe the results of this study will be important in designing an end-effector for a mole-inspired underwater sniffing electronic nose.

Future experimental changes could allow closer comparison to the star-nosed mole's sniffing. The star mimics in our study were flat, with fin-like arms, but one could investigate the effect of changing the angle at which the arms deviate from this plane to form a concatenated cone and mimic the way the star-nosed mole cages the bubbles during sniffing, using rods instead of fins. It is also important to consider the wettability of the mole's appendages, as hydrophobic surfaces are very effective at stabilizing large bubbles [15]. Lastly, the star-nosed mole appendages are flexible and clearly bend when in contact with the bubble. Such effects may increase the stability of the bubble, as the bending of the arms would increase the contact with the bubble and the required force to cause the bubble to escape.

The experiments and theory presented consider only a static case, but the sniffing performed by star-nosed moles is a dynamic event. Future work should consider the effect that the star geometry has on bubble formation and retraction. Specifically, it would be interesting to quantify the delay to pinch-off caused by the star and how the bubble surface is altered during that time-scale, as the sniff duration and bubble surface area are critical in understanding the star-nosed mole's capabilities in capturing odors.

The star geometry is unique to the star-nosed mole, yet the American water shrew and Russian desman have shown similar underwater sniffing capabilities. It is possible that the whiskers of these animals could serve an analogous role to the star-nose in stabilizing the bubble. Moreover, it is likely that a number of other mammals may use this ability to smell underwater. A greater understanding of the mechanisms that stabilize the bubble in underwater sniffing may help in identifying other mammals capable of this intriguing behavior.

VI. CONCLUSION

This study was inspired by the ability of the star-nosed mole to hold onto bubbles much larger than the capillary length. We quantified the stability of the bubble as the angle at which the bubble could be tilted until it was released. Flat discs are poor at stabilizing bubbles. However, bends in the disc or triangular gaps are able to allow bubbles to peek through. These bulges create counterbalance, allowing the disc to be tilted to nearly double the angles of flat discs. We showed that certain gap sizes are optimal, both providing sufficient counterbalance for the bubble, but also preventing the bubble from escaping the gap. This idea of the bubble counter-balancing itself is a novel and simple way to increase a bubble's stability, even if the bubble is of a length-scale much larger than the capillary length. Our study provides one step towards building an underwater sensor based on the use of bubbles to capture odors.

VII. ACKNOWLEDGEMENTS

We acknowledge our funding sources, the Georgia Tech School of Biology, and National Science Foundation CAREER Grant 1255127. T. French from Massachusetts Fish and Wildlife provided a frozen star-nosed mole sample for this study.

[1] John Hall, Alan D. Zaffiro, Randall B. Marx, Paul C. Kefauver, E. Radha Krishnan, Roy C. Haught, and Jonathan G. Herrmann. On-line water quality parameters as indicators of distribution system contamination. *Journal (American Water Works Association)*, 99(1):66–77, 2007.

[2] Kenneth C. Catania. Underwater Sniffing Guides Olfactory Localization in Semiaquatic Mammals. *Annals of the New York Academy of Sciences*, 1170(1):407–412, July 2009.

[3] Kenneth C. Catania. Olfaction: Underwater 'sniffing' by semi-aquatic mammals. *Nature*, 444(7122):1024, December 2006.

[4] Yu F. Ivlev, M. V. Rutovskaya, and O. S. Luchkina. The Use of Olfaction by the Russian Desman (Desmana moschata L.) during Underwater Swimming. *Doklady Biological Sciences*, 452:280–283, February 2013.

[5] Brent A. Craven, Eric G. Paterson, and Gary S. Settles. The fluid dynamics of canine olfaction: unique nasal airflow patterns as an explanation of macrosmia. *Journal of The Royal Society Interface*, page rsif20090490, December 2009.

[6] Alvin U. Chen, Patrick K. Notz, and Osman A. Basaran. Computational and Experimental Analysis of Pinch-Off and Scaling. *Physical Review Letters*, 88(17):174501, April 2002.

[7] John Davidson and Sangjin Ryu. High-speed visualization of soap bubble blowing and image-processing-based analysis of pinch-off dynamics. *Journal of Visualization*, 20(1):53–61, February 2017.

[8] Hideki Tsuge, Yusuke Tezuka, and Masae Mitsudani. Bubble formation mechanism from downward nozzle Effect of nozzle shape and operating parameters. *Chemical Engineering Science*, 61(10):3290–3298, May 2006.

[9] David Qur, Marie-Jos Azzopardi, and Laurent Delattre. Drops at Rest on a Tilted Plane. *Langmuir*, 14(8):2213–2216, April 1998.

[10] Jaroslaw Drelich, Jan D. Miller, and Robert J. Good. The Effect of Drop (Bubble) Size on Advancing and Receding Contact Angles for Heterogeneous and Rough Solid Surfaces as Observed with Sessile-Drop and Captive-Bubble Techniques. *Journal of Colloid and Interface Science*, 179(1):37–50, April 1996.

[11] Viatcheslav V. Berejnov and Robert E. Thorne. Effect of transient pinning on stability of drops sitting on an inclined plane. *Physical Review E*, 75(6), June 2007. arXiv: physics/0609208.

[12] Tung-He Chou, Siang-Jie Hong, Yu-Jane Sheng, and Heng-Kwong Tsao. Drops Sitting on a Tilted Plate: Receding and Advancing Pinning. *Langmuir*, 28(11):5158–5166, March 2012.

[13] A. B. D. Cassie and S. Baxter. Wettability of Porous Surfaces. *Trans. Faraday Soc.*, 46:546–551, 1944.

[14] Siegfried Kehl and Konrad Dettner. Surviving submergedSetal tracheal gills for gas exchange in adult rheophilic diving beetles. *Journal of Morphology*, 270(11):1348–1355, November 2009.

[15] M. R. Flynn and John W. M. Bush. Underwater breathing: the mechanics of plastron respiration. *Journal of Fluid Mechanics*, 608:275–296, August 2008.

[16] Robert N. Wenzel. Resistance of solid surfaces to wetting by water. *Industrial and Engineering Chemistry*, 28:988–994, 1936.

[17] Kenneth C. Catania and Jon H. Kaas. Somatosensory fovea in the star-nosed mole: Behavioral use of the star in relation to innervation patterns and cortical representation. *The Journal of Comparative Neurology*, 387(2):215–233, October 1997.

[18] Pierre-Gilles de Gennes, Francoise Brochard-Wyart, and David Quere. *Capillarity and Wetting Phenomena: Drops, Bubbles, Pearls, Waves*. Springer-Verlag, New York, 2004.

[19] Robert J. Benzing and John E. Myers. Low Frequency Bubble Formation at Horizontal Circular Orifices. *Industrial & Engineering Chemistry*, 47(10):2087–2090, October 1955.

[20] F. P. Bretherton. The motion of long bubbles in tubes. *Journal of Fluid Mechanics*, 10(2):166–188, March 1961.

[21] Sergio Di Bari and Anthony J. Robinson. Experimental study of gas injected bubble growth from submerged orifices. *Experimental Thermal and Fluid Science*, 44:124–137, January 2013.

[22] Subrat Das, Yos S. Morsi, Geoffrey Brooks, John J. J. Chen, and William Yang. Principal characteristics of a bubble formation on a horizontal downward facing surface. *Colloids and Surfaces A: Physicochemical and Engineering Aspects*, 411:94–104, October 2012.

[23] Stanley Hartland and Richard W. Hartley. *Axisymmetric fluid-liquid interfaces*. Elsevier Scientific, Amsterdam, 1976.

[24] T. Maxworthy. Bubble rise under an inclined plate. *Journal of Fluid Mechanics*, 229:659–674, August 1991.

[25] S. J. Gould and R. C. Lewontin. The Spandrels of San Marco and the Panglossian Paradigm: A Critique of the Adaptationist Programme. *Proceedings of the Royal Society of London. Series B, Biological Sciences*, 205(1161):581–598, 1979.

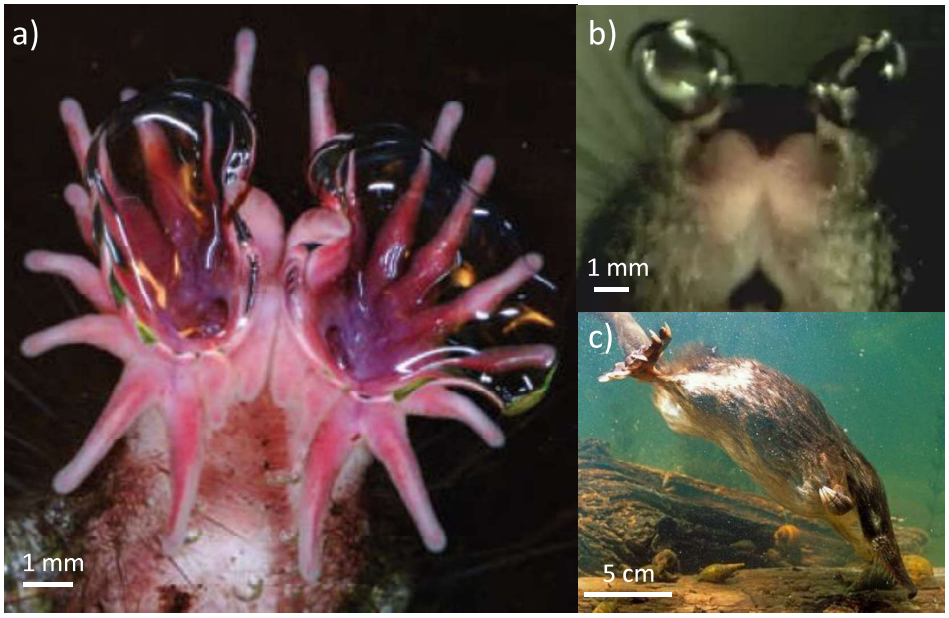

FIG. 1. Three semi-aquatic mammals exhibit underwater sniffing: (a) the star-nosed mole blows a bubble of 0.1 mL on a timescale of 0.1 seconds, (b) the American water shrew blows a bubble of 0.06 mL on a timescale of 0.08 seconds, and (c) the Russian desman blows a bubble of 0.3 mL on a timescale of 0.07 seconds. Photographs (a,b) courtesy of K. Catania. Photograph (c) courtesy of I. Shpilenok.

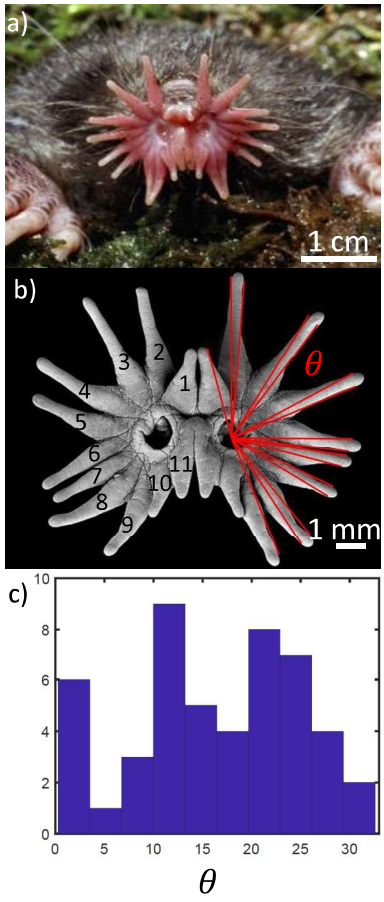

FIG. 2. Geometry of the nose of the star-nosed mole. (a) The star-nosed mole, whose fleshy, star-shaped nose measures approximately 10 mm across. (b) Close up photograph of the nose, with red lines showing how the gap angle θ is measured. The red line is drawn between the center of the nostril and the inside tip of the appendages. (c) Histogram showing the distribution of the gap angles θ for three star-nosed moles. Photograph (a) and (b) courtesy of K. Catania.

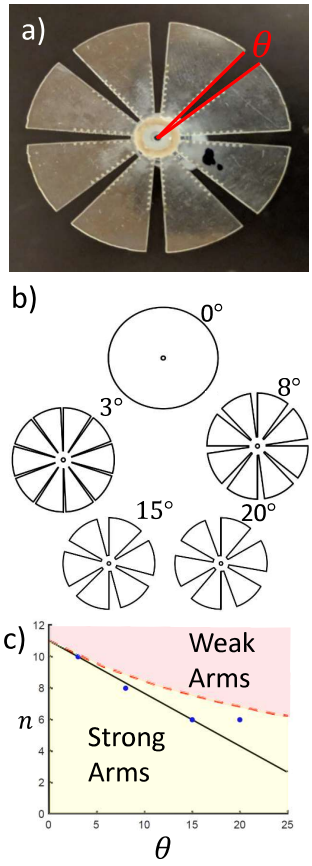

FIG. 3. Design of plastic stars mimicking the star-nosed mole's nose. (a) Plastic stars laser-cut to mimic the star-nose. Like in the photos of star-nosed moles, the gap angle was measured along the inner edges of the arms with the vertex at the center of the nozzle. (b) Schematics of the five plastic stars used in this study. Angles indicate the gap angles for each of the stars. (c) Relationship between the gap angle θ and the number of gaps for each star. The dashed red curve represents the fabrication limitation that the minimum width of each fin is greater than 2 mm. The blue dots are the actual number of gaps used in the experimental stars. The solid black line is a linear approximation used to represent the relationship between the number of gaps and the gap angle for smaller gap angle stars from $3° - 15°$.

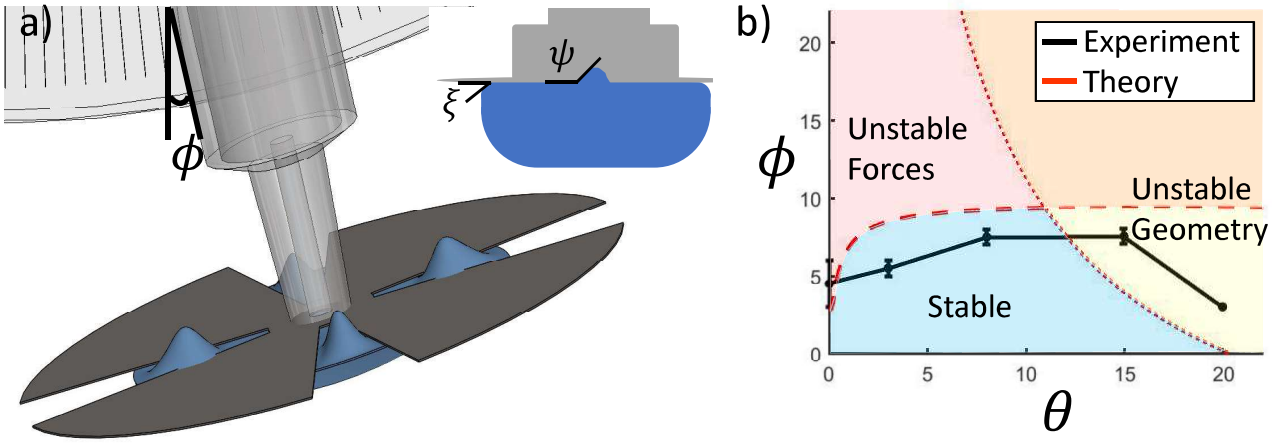

FIG. 4. (a) Schematic of the experimental setup in which a syringe with a plastic star is affixed to a protractor. As a measure of bubble stability, the syringe is tilted at an angle ϕ before the bubble pinches off. Inset shows the contact angle, $\xi = 54°$, of the bubble below the star and the angle, $\psi = 127°$, of the bubble pushing up through the gap. (b)The relationship between the maximum tilt angle ϕ and the gap angle θ of the star. Experimental data (black) suggests an optimal gap angle around $8° - 15°$, and the theory predicts an optimum at $11° \pm 3°$. The theory described in §3 describes a large gap condition leading to pinch-off (red dotted line) and a small gap condition leading to pinch-off (red dashed line).

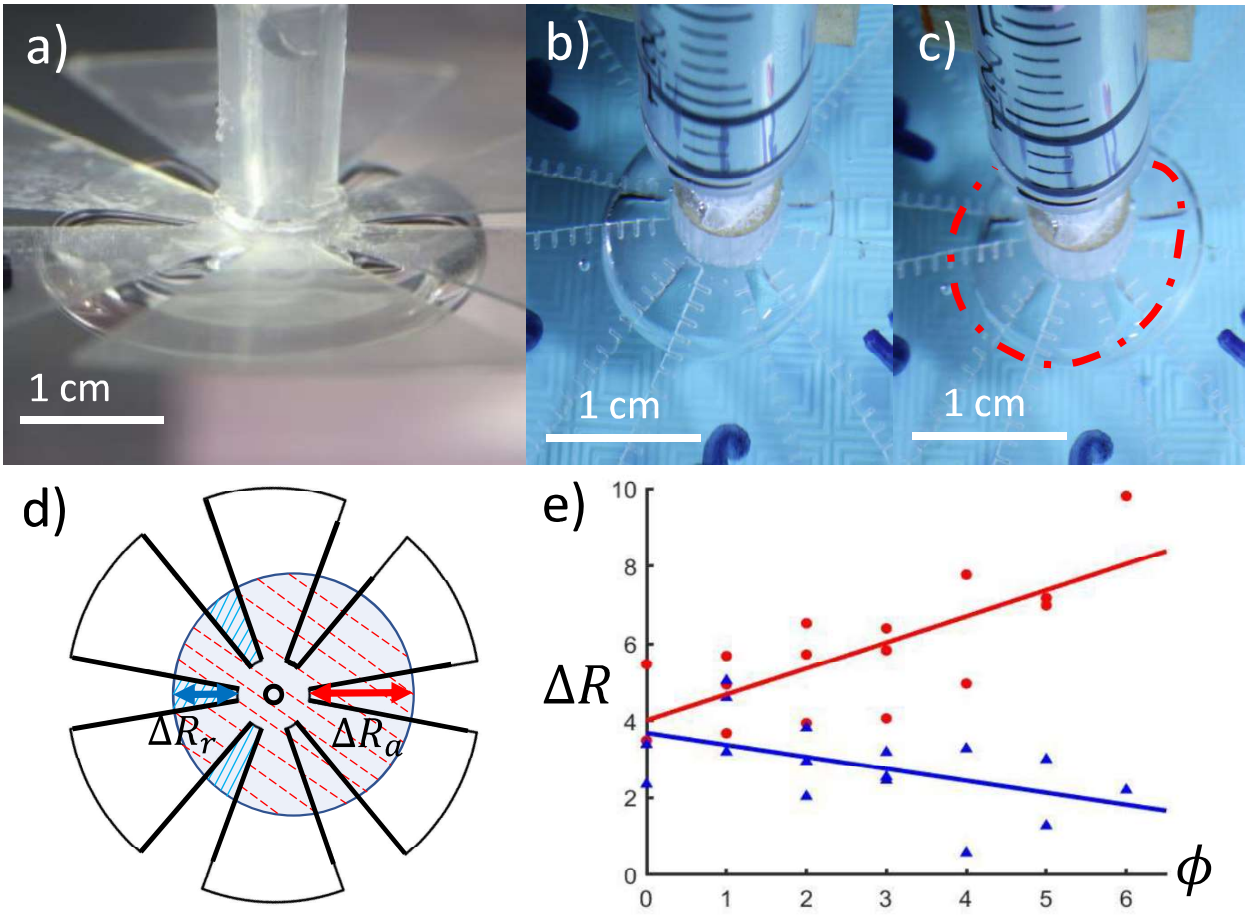

FIG. 5. Position of the bubble with varying tilt angle ϕ. (a) Photograph shows portions of a bubble rising through the gaps between the arms of the star, forming ribs similar to a pumpkin. (bc) Two photographs showing the position of the bubble before and after the star is tilted by an angle of 4°. The red dotted line shows the original position of the bubble. As the system is tilted, one side of the bubble advances, and the other recedes. (d) The shift in bubble position creates two lengths from the start of the gap to the edge of the bubble, ΔR_a and ΔR_r for the advancing and receding sides respectively. (e) The relationship between the the tilt angle ϕ and the position ΔR of the bubbles edge for a star of gap angle $\theta = 8°$. The advancing edge is shown as red dots, the receding edge as blue triangles. The solid lines are linear best fits. The bubble pinches off when the tilt angle $\phi = 8°$.

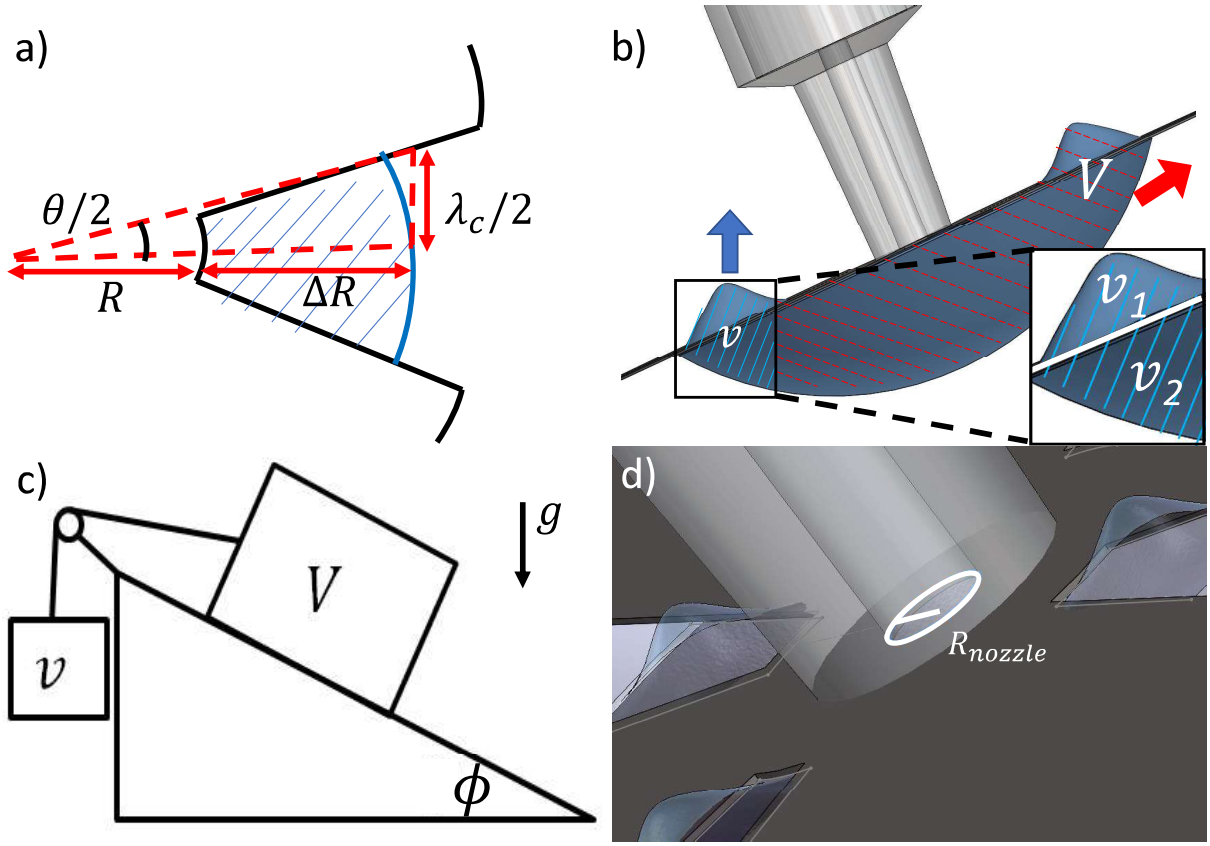

FIG. 6. Illustrations of conditions preventing pinch-off. (a) Schematic of the gap and geometric pinch-off condition for large gap angles. (b) Side view schematics of the bubble interacting with the star shape above it. The buoyancy forces acting on the red region denoted by V are balanced by the buoyancy forces of the blue region of the bubble-star system for small gap angles. The portion of the bubble V (dashed red hashed region) slides off the star while the small portion in the gap, v (solid blue hashed region), acts as a counterbalance, similar to an analogous mass-on-a-ramp system shown in (c). Inset in (b) shows how v is split up into two regions v_1 and v_2 for volume calculations. (d) The parallel buoyant force must overcome the resistive surface tension force between the main bubble and air remaining in the syringe nozzle. Here, the radius R_{nozzle} is labeled.

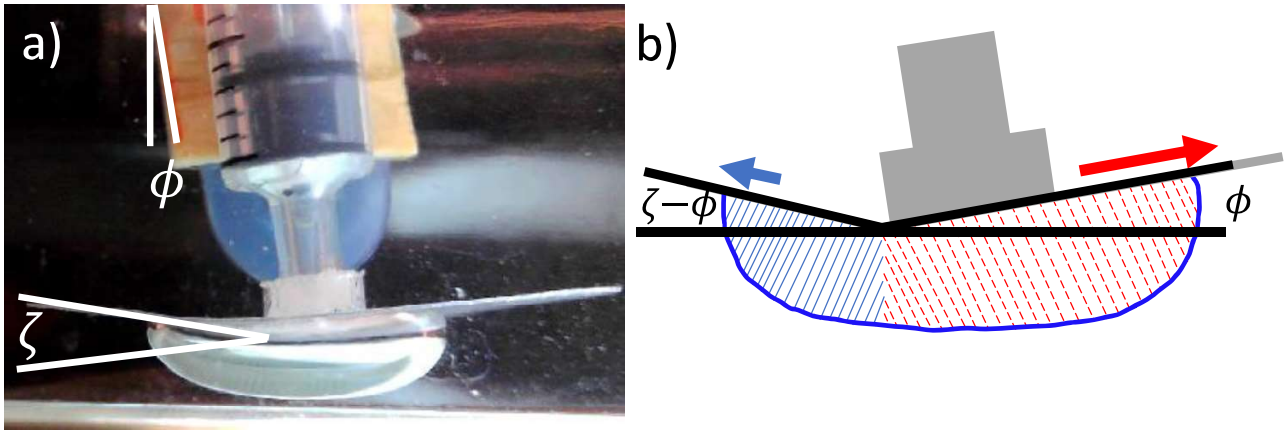

FIG. 7. Schematic diagrams of the geometry of a bent plastic disc. (a) Photograph of the bubble held by the bent star and (b) schematic of the portions of the bubble showing counterbalance. The buoyancy force on the red hashed region causes the bubble to slide to the right. The bubble is held in place by the opposing buoyancy force on the blue hashed region.

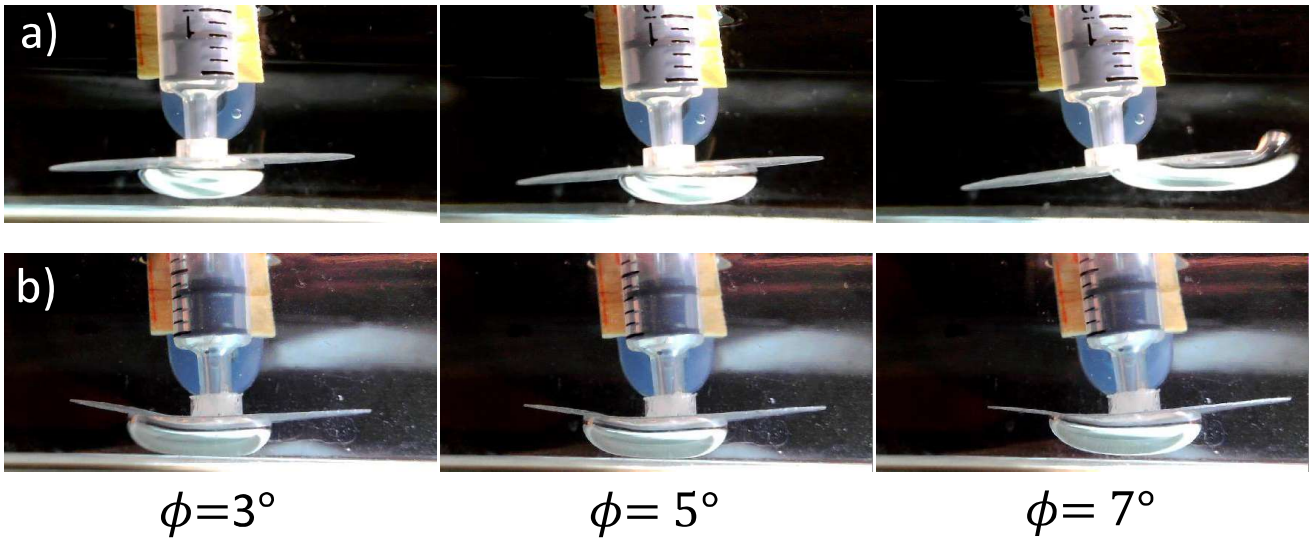

FIG. 8. Experiments demonstrating the ability of a bubble to maintain counterbalance to remain stable. (a) A flat disc can only be tilted to $\phi = 4.5^\circ \pm 1.5^\circ$ before the bubble escapes. (b) A disc with a $\zeta = 15^\circ$ bend at a position off-center can hold onto a bubble up to $\phi = 10^\circ$ of tilt, demonstrating the importance of geometry in maintaining bubbles.